PNAS RESEARCH ARTICLE | BIOPHYSICS AND COMPUTATIONAL BIOLOGY

Quantifying heterogeneity to drug response in cancer–stroma kinetics

Francesco Alemanno[a,b,1], Marta Cavo[a,1], Donatella Delle Cave[c], Alberto Fachechi[d], Riccardo Rizzo[a], Eliana D'Amone[a], Giuseppe Gigli[a,b], Enza Lonardo[c], Adriano Barra[b,e,2], and Loretta L. del Mercato[a,2]

Edited by Michele Castellana, Institut Curie, Paris, France; received December 13, 2021; accepted February 4, 2023, by Editorial Board Member Mehran Kardar

A crucial challenge in medicine is choosing which drug (or combination) will be the most advantageous for a particular patient. Usually, drug response rates differ substantially, and the reasons for this response unpredictability remain ambiguous. Consequently, it is central to classify features that contribute to the observed drug response variability. Pancreatic cancer is one of the deadliest cancers with limited therapeutic achievements due to the massive presence of stroma that generates an environment that enables tumor growth, metastasis, and drug resistance. To understand the cancer–stroma cross talk within the tumor microenvironment and to develop personalized adjuvant therapies, there is a necessity for effective approaches that offer measurable data to monitor the effect of drugs at the single-cell level. Here, we develop a computational approach, based on cell imaging, that quantifies the cellular cross talk between pancreatic tumor cells (L3.6pl or AsPC1) and pancreatic stellate cells (PSCs), coordinating their kinetics in presence of the chemotherapeutic agent gemcitabine. We report significant heterogeneity in the organization of cellular interactions in response to the drug. For L3.6pl cells, gemcitabine sensibly decreases stroma–stroma interactions but increases stroma–cancer interactions, overall enhancing motility and crowding. In the AsPC1 case, gemcitabine promotes the interactions among tumor cells, but it does not affect stroma–cancer interplay, possibly suggesting a milder effect of the drug on cell dynamics.

pancreatic cancer | cross talk | chemotherapy | statistical mechanics | stochastic processes

Cell–cell interaction in complex multicellular organisms is an intricate phenomenon affected by specific physiological environments (1). This interplay is pivotal in maintaining tissue organization and homeostasis, so as to coordinate an appropriate response to dangerous perturbations. When these dialogues go wrong, diseases may rise: The best example is cancer, which can be defined as a social dysfunction within the cellular community (2) and used as a model system to study intercellular communications. Modeling and predicting cellular interactions which provide insight into the mechanism of disease development and progression is thus of utmost importance (3–5).

A benchmark case is the interplay between pancreatic ductal adenocarcinoma (PDAC) cell lines and pancreatic stellate cells (PSCs) since their mutual interaction is known to be critical for PDAC progression (6, 7): In this setting, many efforts have been devoted to assessing whether soluble mediators produced by carcinoma cells stimulated motility, proliferation, and matrix synthesis of PSCs and how these interactions enhance tumor growth and progression (8–10). A major part of the literature affirms that chemoresistance in PDAC is partially due to a unique presence of fibrous, stiff extracellular matrix (desmoplasia) surrounding the tumor, that could affect the intratumoral drug penetration (11). However, the role of desmoplasia in cancer progression is complex and remains somehow controversial; in 2014, Gore and Korc went through the available literature trying to clarify whether the stroma is a friend or foe in PDAC (12): Indeed, in that period, several studies had demonstrated how targeting the stroma resulted in undifferentiated and more aggressive pancreatic cancer (13, 14). Desmoplasia mainly derives from PSCs that are activated to proliferate and produce collagens, laminin, and fibronectin (15); consequently, besides the physical role played by desmoplasia, another key aspect to consider is the molecular cross talk between stroma and tumor cells, that regulates each cell type's survival, migration, and other protumorigenic properties. The lack of proper experimental models and approaches for inspecting this cross talk contributed to enhancing poor knowledge related to PDAC underlying mechanisms. Indeed, despite the need to study the complex interactions between PDAC cells and PSCs, very limited in vitro options currently exist (16, 17). A possible reason is

Significance

Cell–cell interactions are crucial for organism survival, yet inferring intercellular signaling pathways—ranging from chemical messenger to direct contact—is challenging, as it mainly relies on biochemical and genetic analyses. We develop a computational method that requires solely time-lapse fluorescence microscopy to quantify effectively these interactions and their effects on cellular dynamics. We compute interactions among stroma cells and pancreatic ductal adenocarcinoma cells by comparing their dynamics in presence of the chemotherapeutic drug vs. the control case, unraveling variations in cancer–stroma kinetics and quantifying the heterogeneity to drug response in an in vitro coculture model. This approach can also be used to monitor cell kinetics under different cellular perturbations, thus representing a powerful tool with a broad spectrum of applications in computational biology.

The authors declare no competing interest.

This article is a PNAS Direct Submission. M.C. is a guest editor invited by the Editorial Board.

[1]F.A. and M.C. contributed equally to this work.

[2]To whom correspondence may be addressed. Email: adriano.barra@unisalento.it or loretta.delmercato@nanotec.cnr.it.

This article contains supporting information online at http://www.pnas.org/lookup/suppl/doi:10.1073/pnas.2122352120/-/DCSupplemental.

Published March 10, 2023.

that the study of cell dynamics, from direct cellular contact to soluble mediators, is complicated as it usually involves advanced techniques ranging from gene expression analyses to coimmunoprecipitation, proximity labeling proteomics, fluorescence resonance energy transfer imaging, X-ray crystallography, and more (18).

Here, restricting to signaling affecting the cell's kinetics, we present a cheap computational approach that allows quantifying the existence and intensity of interactions ruling the cell's dynamics: In a nutshell, via standard fluorescence microscopy imaging and cell tracking, we collect the phase space of the experiment, namely, the ordered time series of all the cell's positions and velocities. This information constitutes the input of our computational protocol, that returns as output the effective intensity of interactions among the various cells and an exhaustive quantitative description of their dynamics. Note that the method can predict the existence and effective magnitude of the interaction but not its biological nature. Yet, despite this limitation, this approach can compare how different drugs affect the kinetics of the same ensemble of cells; hence, it can play as a tool to quantify kinetic cancer's drug response.

Specifically, we preliminary evaluate the effect of two PDAC cell lines on PSCs kinetics by performing a standard wound-healing assay: We make a scratch in a monolayer of PSCs and then expose the cells to a control medium or conditioned medium of L3.6pl or AsPC1 cells for a period of 42 h. As shown in Fig. 1 *A* and *B*, PSCs' migration is heterogeneously affected upon AsPC1 or L3.6pl conditioned media administration, suggesting the dependency of the dynamic behavior of PSCs from factors secreted by tumor cells, thus highlighting the existence of specific cells' interactions. En route toward their quantification, we then perform the following comparative tests: For each tumor cell (i.e., AsPC1 or L3.6pl), we mix the PDAC cells with the PSCs homogeneously to inspect i) how cells orchestrate their coordination (i.e., how they interact) to form larger aggregates and ii) whether and how PSCs infiltrate these aggregates. We then repeat the experiments by adding in the medium 5 μM of gemcitabine. By comparison among the two series of experiments, we infer the role of the chemotherapeutic treatment in tumor–stroma kinetics.

In these experiments, drug vs no-drug, (Fig. 1*C*) tumor cells are left to freely interact with PSCs, keeping the ratio 25% of pancreatic tumor cells ("tumor" from now on) and 75% of PSCs pancreatic stellate cells ("stroma" from now on). The tumor and stroma cells are labeled with different fluorescent tracking dyes for time-lapse confocal imaging (*Methods* for further details) to produce two distinct datasets containing all the cell's positions at given time points (Fig. 1*D*) and thus, by differentiating two consecutive time frames, also the cell's velocities, namely the "phase space" of the whole experiment (Fig. 1*E*) that is the input of the computational protocol (Fig. 1 *F* and *G*).

To obtain a clear scenario of the cell's kinetics, the key observable to investigate is the cell's velocity: We split the study of this vector by analyzing its direction by means of maximum-entropy statistical analysis and its modulus by means of stochastic processes theory. By the former, we infer the existence and magnitude of interactions among cells; by the latter (taking advantage of the homogeneous initial state), we inspect whether and how the two cellular populations tend to form aggregates, to mix e.g., stroma can infiltrate within the tumoral clumps (19), etc. Finally, a third and independent correlation analysis guarantees overall coherence and reliability of the results. These are obtained by merging outcomes of these three approaches (reported one per section in the following): Comparing experiments with and without gemcitabine, we finally conclude on the role of the drug in governing the overall kinetics under investigation.

On the Cell's Sensing and Interactions. Interactions can be inferred by studying the directional aspects of the cell's velocities: As standard in this case (20–22), we study the normalized orientational order parameter

$$\hat{n}_i(t) := \frac{\vec{v}_i(t)}{||\vec{v}_i(t)||} = \frac{\vec{r}_i(t+\Delta t) - \vec{r}_i(t)}{||\vec{r}_i(t+\Delta t) - \vec{r}_i(t)||},$$

defined as the velocity $\vec{v}_i(t)$ of a given cell i at time t divided by its modulus, namely, the angle tracing the orientation, or simply the direction of that cell. Do the cells tend to cooperate, to align, or, rather, to move independently? And how their coordination—if any—is affected by the drug? To answer these questions, we need to know the collective properties of the cell's directions, probabilistically coded by some unknown probability distribution $P(\hat{n})$ that we aim to find out by maximum entropy analysis (20).

Given a dataset $\hat{n} = \hat{n}_1(1), ..., \hat{n}_i(t), ..., \hat{n}_N(T)$ (composed of multiple observations of the quantity $\hat{n}_i(t)$ from $t = 1$ to $t = T$ and for all the cells we track, i.e., $i \in (1, ..., N)$), this approach allows reconstruction of the probability distribution $P(\hat{n})$ from a limited number of empirical observations (too small to reconstruct the probability distribution directly from the data) by requiring such a probability distribution to reproduce all the experimental measurements yet being minimally structured, in a standard Occam razor way (namely, at the maximum entropy).

Using the labels S and T for stroma and tumor respectively, we need the inferred probability distribution to predict correlations that match the measured ones, namely, empirical one-point $C_1(\hat{n}^S)$, $C_1(\hat{n}^T)$ and two-point $C_2(\hat{n}^S, \hat{n}^S)$, $C_2(\hat{n}^T, \hat{n}^T)$, $C_2(\hat{n}^S, \hat{n}^T)$ correlation functions (*SI Appendix* for their definition). To find $P(\hat{n})$ explicitly, we introduce the following Lagrange multipliers (that force the entropy to produce this matching): a *coupling* J_S (resulting from the constraint on $C_2(\hat{n}^S, \hat{n}^S)$ that accounts for stroma–stroma interactions), a *coupling* J_T (resulting from the constraint on $C_2(\hat{n}^T, \hat{n}^T)$ that accounts for tumor–tumor interactions), and a mixed coupling J_M (resulting from the constraint on $C_2(\hat{n}^S, \hat{n}^T)$ that accounts for mixed interactions among stroma and tumor cells). The values of these couplings have to be inferred from data, and should they result positive (negative), they would imply a positive (negative) effective interaction, while zero values represent the absence of interaction. Further, $\mathbf{H}_S = (H_{S,x}, H_{S,y})$ and $\mathbf{H}_T = (H_{T,x}, H_{T,y})$ are two bidimensional extraparameters (i.e., simple homogeneous external fields) that we should include to deal with a possible persistency coded in the one-point correlation functions $C_1(\hat{n}^S)$, $C_1(\hat{n}^T)$; see the cartoon in Fig. 2*A* to capture the meaning of the various parameters. We refer to *SI Appendix* for a detailed explanation of the maximum entropy principle (in particular, Sec. 1.A for its construction suitable for the present analysis, *SI Appendix*, section 1.B for the related resolution, and *SI Appendix*, section 1.C for its extensive synthetic validation).

The extremization of the Shannon entropy returns $P(\hat{n})$ as the Boltzmann–Gibbs distribution of a cost function

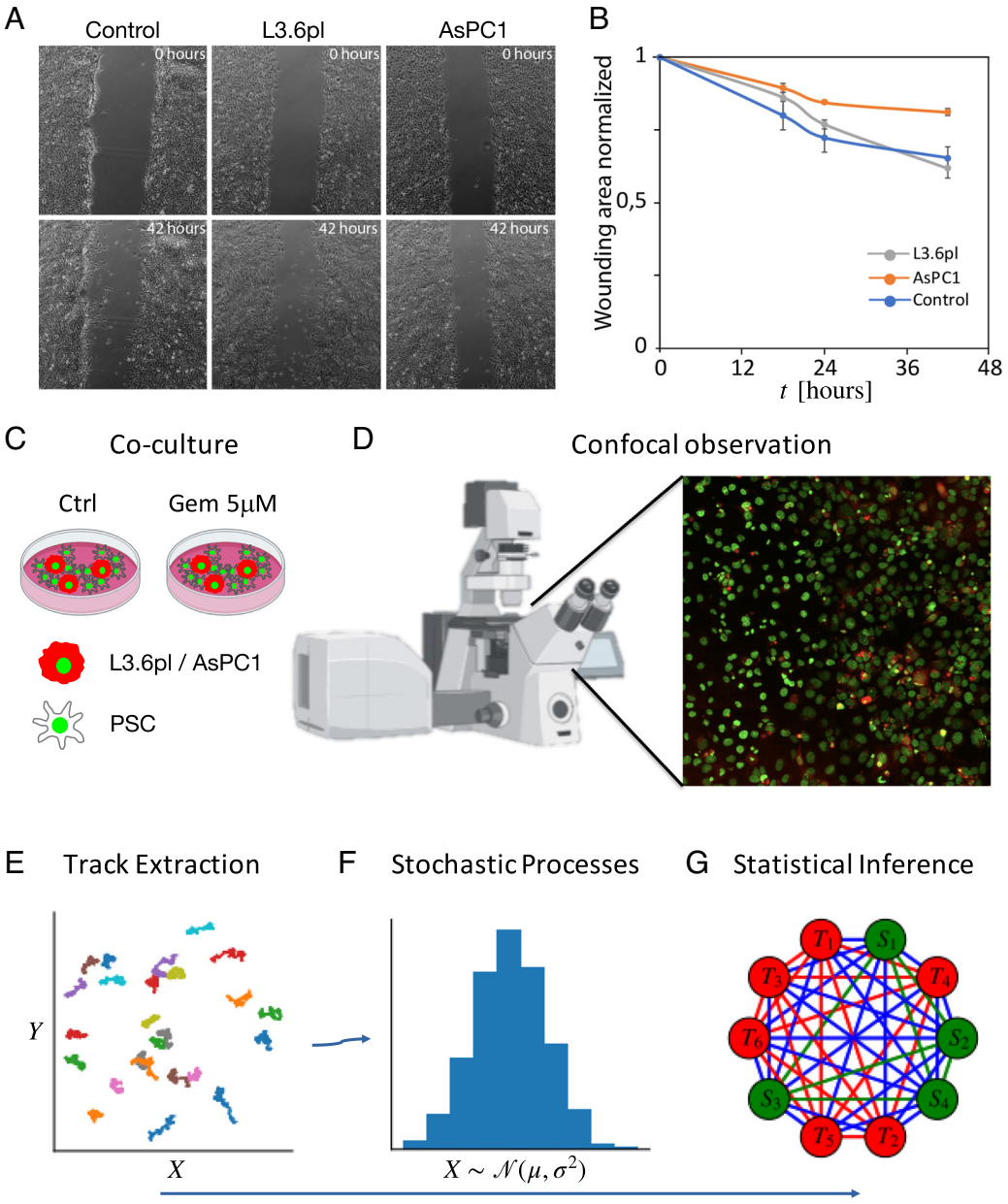

Fig. 1. Cartoon depicting the whole experimental and computational setups. In the first row, we inspect how PSCs migrate in a wound-healing assay with 2D indirect coculture (panel *A*). PSCs were grown in a cell monolayer and exposed, after a scratch, to a conditioned medium from AsPC1 or L3.6pl cells. As shown in panel *B*, where the vertical axes quantify the ratio between the area of the scratch and the total area, the contaminated medium sensibly affects cell migration, confirming the presence of information exchanges among the various cellular lines. Prompted by this preliminary check, we define the following protocol to quantify such interactions: PDAC tumor cells (L3.6pl or AsPC1, red symbols) and stromal cells (PSC, green symbols) are cocultured in a cell culture dish with or without gemcitabine (5 μM) up to 58 h (panel *C*); time-lapse confocal fluorescence microscopy is applied to track the positions of the cells vs. time (panel *D*); trajectories of each cell are reconstructed and, by temporal differentiation, the whole phase space of the experiment is acquired (panel *E*), namely, the time-ordered series of all the cell's positions and velocities: This information is the input to our algorithmic approach, split in stochastic process analysis (panel *F*) and maximum-entropy statistical inference (panel *G*). A last check based on correlation analysis ensures the correctness and global coherence of the results.

$\mathcal{H}(\hat{n}_S, \hat{n}_T | J_S, J_T, J_M, H_S, H_T)$ that is an explicit function of these couplings $\{J_S, J_T, J_M\}$ and fields $\{H_S, H_T\}$ and that reads as

$$P(\hat{n}) = \frac{1}{Z(J,H)} \exp\left(-\mathcal{H}(\hat{n}_S, \hat{n}_T | J, H)\right) \quad [1]$$

$$\mathcal{H} \sim \frac{-1}{N(N-1)} \left[\sum_{i \neq j}^{N_S, N_S} J_S \hat{n}_i^S \hat{n}_j^S + \sum_{i \neq j}^{N_T, N_T} J_T \hat{n}_i^T \hat{n}_j^T + \sum_{i \neq j}^{N_S, N_T} J_M \hat{n}_i^S \hat{n}_j^T \right] - \frac{1}{N} \left(\mathbf{H}_S \cdot \sum_i^{N_S} \hat{n}_i^S + \mathbf{H}_T \cdot \sum_j^{N_T} \hat{n}_j^T \right), \quad [2]$$

where $N = N_S + N_T$, and $Z(J,H)$, the partition function (23), acts as the normalization of $P(\hat{n})$: We obtained a cost-function of a bipartite Heisenberg–Kuramoto model (22, 24).

Hereafter, we report the values of these parameters as resulted from the inference. In the first two rows of Fig. 2, beyond the picture in panel *A*, we present results on synthetic datasets generated accordingly to the Heisenberg–Kuramoto and Vicsek models (*SI Appendix* for details) to calibrate the computational machinery: The maximum entropy analysis reconstructs with high accuracy the (known) values of the drifts H (Fig. 2 *B* and *C*) as well as of the interactions (Fig. 2, panels *D*, *E*, and *F* respectively, for $J_T, J_M,$ *and* J_S). In the third and fourth rows of

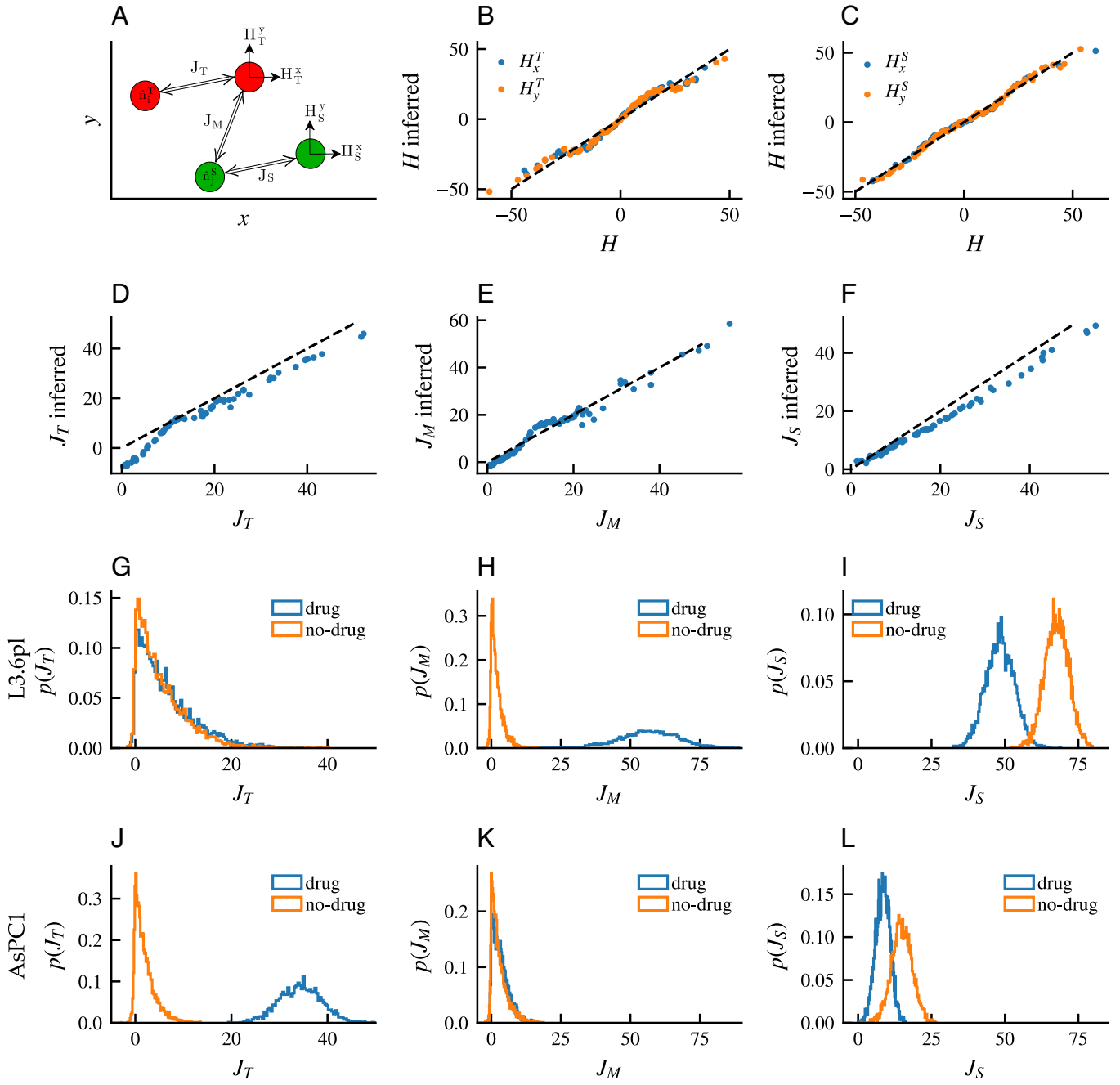

Fig. 2. Inferring the interactions via maximum entropy technique. Panel *A*: Cartoon stylizing two cells per cellular lineage (different lineages in different colors) interacting via the three possible couplings J_T (tumor–tumor interactions), J_S (stroma–stroma interactions), and J_M (mixed interactions tumor–stroma) and, eventually, perceiving a planar field (e.g., a chemotactic gradient) H_x, H_y. Panels *B*–*F*: results of the maximum entropy inference on synthetic datasets simulated by the Heisenberg–Kuramoto model. We simulated 20,000 synthetic trajectories—whose parameters were known—and analyzed their phase space. We plot on the horizontal line the true value of the parameters and on the vertical line the inferred ones. In particular, external fields are reported in panels *B* and *C*, while the interactions among tumor–tumor, tumor–stroma, and stroma–stroma are reported in panels *D*, *E*, and *F* respectively. Panel *G*–*I*: Results from the L3.6pl experiments: distributions of the inferred couplings in the two datasets (without the drug in orange and with the drug in blue). While J_T is roughly left invariant by the drug (panel *G*) and stable on low intensities (suggesting poor tumor–tumor interactions), J_M is by far increased (panel *H*), and J_S is sensibly decreased (panel *I*) by the presence of gemcitabine, the whole suggesting that an effect of the drug is to diminish stroma–stroma interactions and to enrich mixed ones. Panel *J*–*L*: Results from the AsPC1 experiments: distributions of the inferred couplings in the two datasets (without the drug in orange and with the drug in blue). While J_T is sensibly increased by the presence of the drug (panel *J*), mixed interactions are almost absent with or without the drug (panel *K*), and stroma–stroma interactions mildly leveraged by the drug.

Fig. 2 *G*, *H*, and *I* as well as panels *J*, *K*, and *L*, respectively, we report the distributions of the key parameters J_T, J_M, *and* J_S for the L3.6pl and the AsPC1 cases: By inspecting these plots, we conclude that

- Interactions among L3.6pl cancerous cells are not influenced by the drug (panel *G*), while interactions among AsPC1 cancerous cells are strongly enhanced by the drug (panel *J*), highlighting a significant heterogeneity these cells manifest in the kinetic response to gemcitabine.
- Interactions between stroma cells and L3.6pl cancerous cells are deeply influenced by the drug (panel *H*): In particular, without gemcitabine, there are roughly no interactions among stroma and tumor, while in the presence of the drug, pronounced

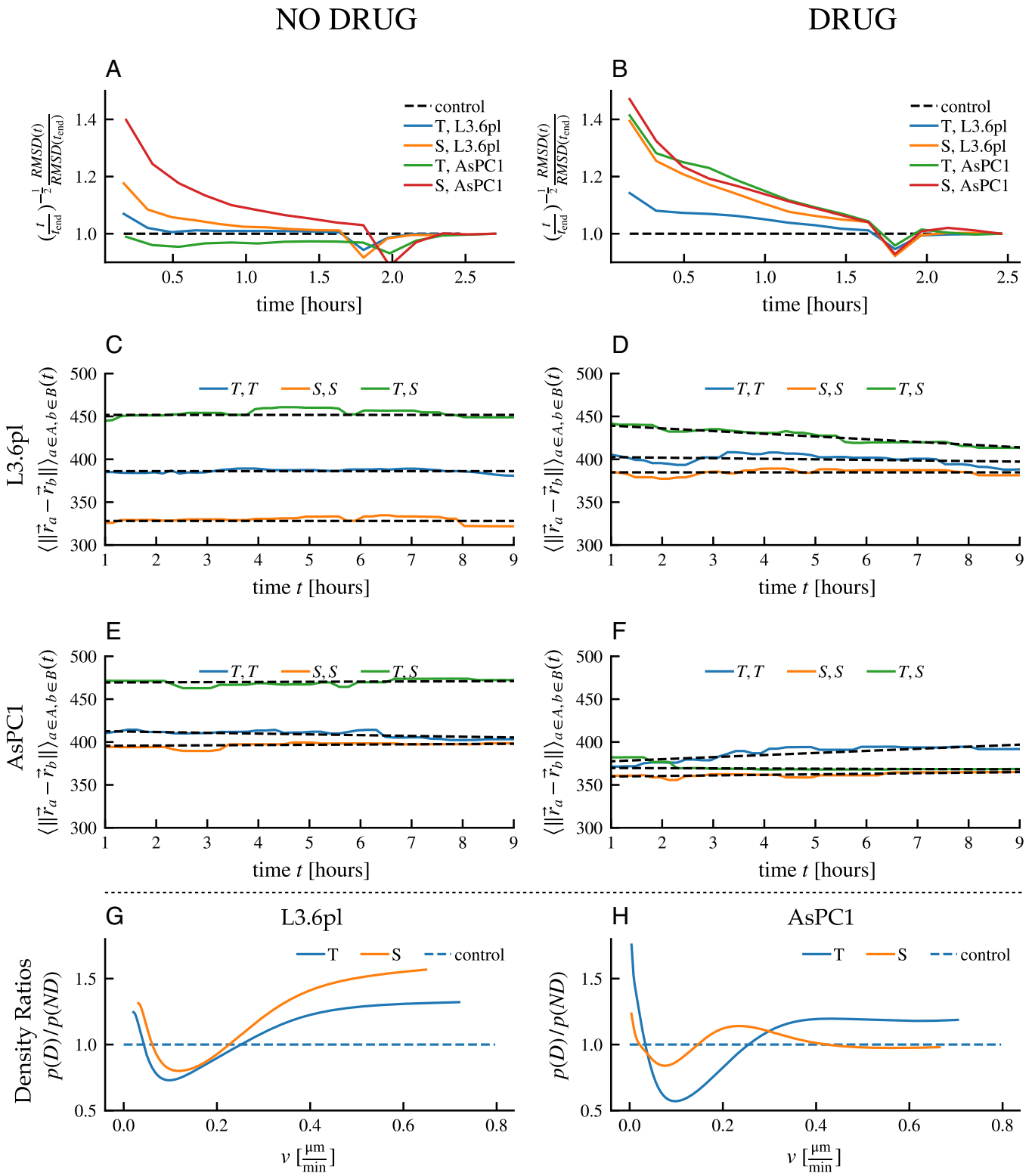

Fig. 3. Evolution of the average intercellular distances (ICD) versus time. First line panels: Ratio of the root mean square displacement over a standard diffusion $\langle x^2 \rangle \sim t$ for both tumor (blue) and stromal (orange) cells (dataset with the drug: panel *A*; dataset without the drug: panel *B*. The control (dashed black line) is the Brownian pure diffusion reference. Second line panels: Distributions, for the L3.6pl case, of mean intercellular distances $D_{T,T}(t)$, $D_{T,S}(t)$, *and* $D_{S,S}(t)$ (Eq. **3**). Dataset without the drug: panel *C*; dataset with the drug: panel *D*. The trajectories, that are almost ballistic, show drastic differences in the evolution of these quantifiers over time: Overall, in the dataset with gemcitabine, cells show sensibly more activity and more capacity of reducing relative intercellular distance with respect to the cells belonging to the dataset without the drug, suggesting that—due to gemcitabine—the two different populations of cells tend to stick together (i.e., $D_{T,S}(t)$ is a monotonic decreasing function in time). Third line panels: Distributions, for the AsPC1 case, of mean intercellular distances $D_{T,T}(t)$, $D_{T,S}(t)$, $D_{S,S}(t)$ (Eq. **3**). Dataset without the drug: panel *E*; dataset with the drug: panel *F*. The main difference with respect to the L3.6pl counterpart is that $D_{T,S}(t)$ no longer decreases in time. It remains roughly constant (suggesting that dialogues among different cell lines are not pronounced in this case); further, $D_{T,T}(t)$ mildly increases over time. Note that the different offsets in panels *C*–*F* are due to the heterogeneous initial state obtained by mixing the two cellular lines and do not contain relevant information on crowding. Fourth line panels: Ratio among the distributions of the velocities (distribution of velocities in the presence of the drug over distribution of velocities in the absence of the drug) for the L3.6pl case (panel *H*) and the AsPC1 case (panel *H*): We highlight that, while in panel *G* both the stroma and the tumor acquire motility (as both the orange and blue curve are above one for higher values of velocity v), this does not happen in the AsPC1 case, where solely the tumoral line acquires motility.

interactions do appear. On contrary, for the AsPC1 case, there are no net mixed interactions neither without nor with the drug (panel *K*).

- Interactions within the stroma are impaired by the drug: For the L3.6pl scenario (panel *I*) this is manifest; PSCs sensibly diminish to interact reciprocally in the presence of gemcitabine (possibly to enhance interactions with the cancerous counterpart). This appears mildly in the AsPC1 case too, as reported in panel *L*.

As last remarks on this approach, we note that we worked in a Bayesian setting (25) to allow evaluating the errors affecting the estimates of the parameters directly providing their probability distributions (Fig. 2 and *SI Appendix*). However, we also stress that, beyond the reward of a useful picture capturing effective cells' interactions, their interpretation should be done with great care as these are not real interactions but just the result of the correlations kept in the extremization (see e.g., refs. 23, 26–28 and references therein): Indeed, maximum entropy approaches return Boltzmann–Gibbs distributions of cost functions that lack a Hamiltonian interpretation, further they possibly offer room for criticism as their absence of assumptions may result unreasonable (21, 29).

On the Cell's Diffusion and Crowding. As the two types of cells are homogeneously mixed together, there is no global chemotactic gradient neither in the experiment with no-drug (ND) nor in the one with the drug (D); hence, in the long-run limit, cells should overall perform Brownian motion (their dynamics is expected asymptotically diffusive): This is confirmed in the first row of panels in Fig. 3 where we show the temporal evolution of the ratio between the empirical root mean square displacement of the two lineages and that of a pure Brownian diffusion (the control in the panels) for both the datasets, without the drug (panel *A*) and with the drug (panel *B*). While on the short timescale, cells deviate from pure diffusion (and actually their motion can be locally ballistic); for long-enough times, the two collapse on the control (as deepened in *SI Appendix*, sections 2.A and 2.B).

However, looking at shorter times, it is also evident that interactions among cells take place and that these are enhanced by the presence of the drug: To inspect their effects, e.g., whether and how cells thicken, we study the average intercellular distance $D(t)$, as a function of time t, defined as

$$D_{A,B}(t) = \langle ||\vec{r}_a(t) - \vec{r}_b(t)|| \rangle_{a\in A, b\in B}, \quad [3]$$

where the averages are restricted to the cellular type such that $A = (S, T)$ and $B = (S, T)$ giving rise to three quantifiers: $D_{S,S}(t)$, $D_{S,T}(t)$, and $D_{T,T}(t)$.

If there is no crowding, these quantifiers are expected to fluctuate around constant values over time; conversely, if S and T types are merging, $D_{S,T}(t)$ should be a monotonously decreasing function (likewise, if those cells are spreading away, $D_{S,T}(t)$ is expected to increase in time). These markers are depicted in the second row of panels in Fig. 3 for the L3.6pl case for both the datasets, without the drug (panel *C*) and with the drug (panel *D*) and in the third row of panels in Fig. 3 for the AsPC1 case for both the datasets, without the drug (panel *E*) and with the drug (panel *F*).

Remarkably, for the L3.6pl scenario, while $D_{S,S}(t)$ remains (approximately) constant in both the experiments, $D_{S,T}(t)$ and $D_{T,T}(t)$ are (approximately) constant solely in the dataset without the drug, while in the presence of gemcitabine, these are monotonically decreasing functions of time. In particular, $D_{S,T}(t)$ significantly experiences this phenomenon, suggesting that while tumor cells tend to form agglomerations also, stromal ones tend to join in due to the presence of the drug. This is no longer true in the AsPC1 counterpart where $D_{S,T}(t)$ stays constant even in the presence of the drug.

We also highlight that, while the motion of these cells is globally diffusive at the macroscale (Fig. 3 *A* and *B* and deepened in *SI Appendix*), local interactions give rise to ballistic motion, typical of sensing cells (22, 30) as the best fit for their (average) reciprocal distances vs. time returns roughly linear dependence of time for $D_{A,B}(t)$ vs. t: A local ballistic shortage suggests that the T and S lineages are actually interacting, as it happens in the L3.6pl case (Fig. 3*D*) in complete agreement with the inferential outcomes by maximum entropy extremization of the previous section.

Further, we plot the ratio among the velocity distributions pertaining to the stroma and to the tumor in the presence vs.

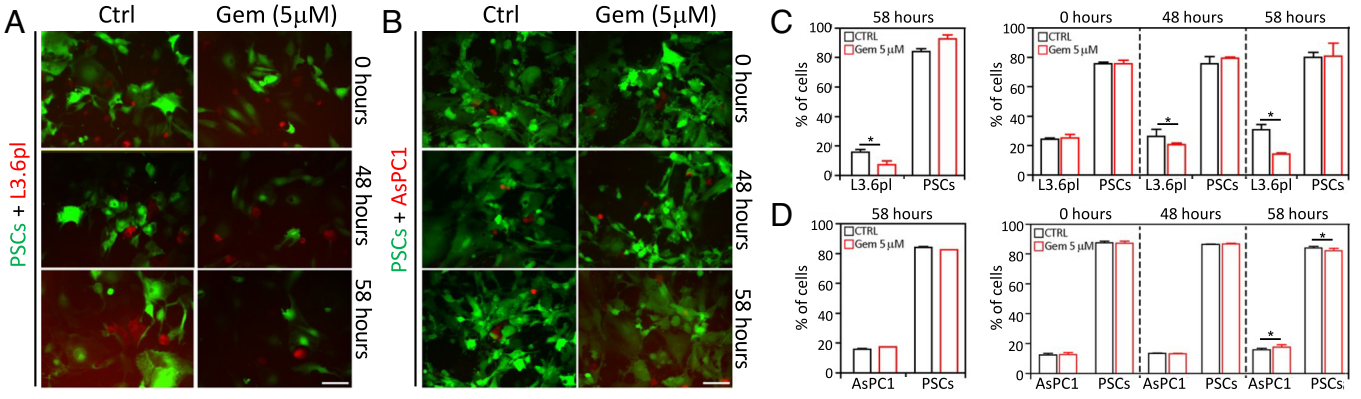

Fig. 4. Fluorescence imaging of tumor–stroma cocultures during chemotherapy and evaluation of cell proliferation. Panel *A* Representative fluorescence images of L3.6pl cells (red) cocultured with PSCs (green), in the presence or absence of 5 μM gemcitabine (Gem) for 0, 48, and 58 hours. (Scale bars, 100 μm.) Panel *B* Representative fluorescence images of AsPC1 cells (red) cocultured with PSCs (green), in the presence or absence of 5 μM Gem for 0, 48, and 58 h. (Scale bars, 100 μm.) Panel *C*) Percentage of L3.6pl and PSCs after treatment with 5 μM Gem, counted with the hemocytometer (*Left* graph) or with the flow cytometer (*Right* graph) at the indicated times. $n \geq 3$. Panel *D*) Percentage of AsPC1 and PSCs cells after treatment with 5 μM Gem, counted with the hemocytometer (*Left* graph) or with the flow cytometer (*Right* graph) at the indicated times. $n \geq 3$; $P \leq 0.05$.

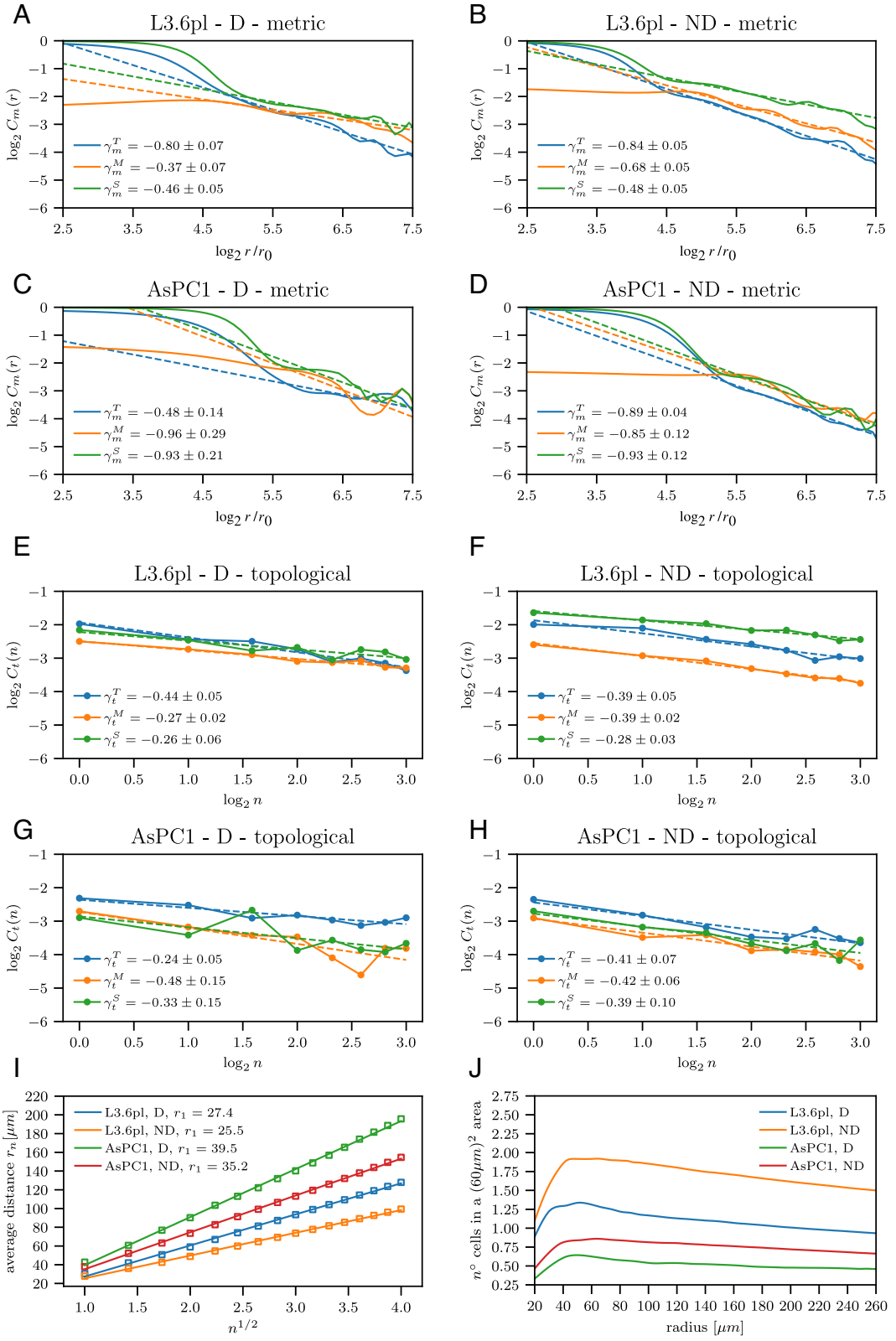

Fig. 5. Metric vs. topological correlations. Panels *A-D* Metric correlation functions for both the cellular lines (L3.6pl and AsPC1) and the drug (D)/nondrug (ND) cases as reported in the titles. $r_0 = 1\,\mu$m. Best fits are provided with $C_m(r) \propto r^{\gamma m}$ (the three values of γ_m are reported for TT interactions γ_m^T, TS interactions γ_m^M, and SS interactions γ_m^S). Panels *E–H* Topological correlation functions for both the cellular lines (L3.6pl and AsPC1) and the drug (D)/nondrug (ND) cases as reported in the titles. Best fits are provided with $C_t(n) \propto n^{\gamma t}$ (the three values of γ_t are reported for TT interactions γ_t^T, TS interactions γ_t^M, and SS interactions γ_t^S). Panel *I*) Mean distance of the nearest neighbors for both the cellular lines (L3.6pl and AsPC1) and the drug (D)/nondrug (ND) cases as reported in the legend. Linear best fits are provided with $r_n = r_1\sqrt{n}$, r_1 accounting for the mean nearest-neighbor distance. The inferred values of r_1 are reported in the legend for the various cases. Panel *J* Cellular density plot returning the mean number of cells sampled in a $60\,\mu m^2$ area within a given distance r: Note that all the curves share the maximum roughly slightly above a mean cellular diameter (i.e., $\epsilon \sim 40\,\mu$m) highlighting the presence of clumps (this point is deepened in the last section of *SI Appendix*).

absence of the drug, i.e., the ratio "(drug distribution)/(no drug distribution)" for both stromal and tumor cells (panel *G* for the L3.6pl case and panel *H* for the AsPC1 case): In the L3.6pl kinetics, the effect of gemcitabine is to speed up the cells above a threshold (that is slightly different between S and T cells resulting in $\sim$0.3 μm/min and 0.2 μm/min, respectively), and this phenomenon is sensibly more pronounced for the stroma (the latter is possibly approaching cancerous clumps, coherently with the rise of the mixed interactions inferred in the previous section; Fig. 2*H*). In the AsPC1 counterpart, instead, stroma dynamics results almost unaffected by the presence of gemcitabine also from this perspective (coherently with Fig. 2*K* where mixed interactions have not been detected). Finally, we correlate the outcomes of the effects of the drug by counting live/dead cells by flow cytometry: As presented in Fig. 4, 5 μM gemcitabine decreased L3.6pl cell proliferation (roughly $\sim$50%) as compared to the control group (Fig. 4 *A* and *C*), but it did not affect AsPC1 proliferation (Fig. 4 *B* and *D*). Manual and automatic counting of dead and live cells (*Methods* for further details) showed that the stromal cell population resulted highly resistant to the treatment.

On the Nature of the Correlations. Following (31, 32), we now develop a systematic study of metric vs. topological correlations to confirm results achieved by previous inspections and to deepen the understanding of whether the inferred interactions are mainly ruled by metric or topological distances.

The metric correlation function measures the reciprocal influence of all the cell's couples of the type (A,B)—where (A,B) can be tumor–tumor (T), mixed stroma–tumor (M), or stroma–stroma (S)—that lie within a distance $\sim r$, and it is defined as

$$C_m^{T\vee M\vee S}(r)=\left\langle \frac{\sum_{i\in A,j\in B}^{TT\vee TS\vee SS}\hat{n}_i(t)\cdot\hat{n}_j(t)\delta_\epsilon(r-r_{ij})}{\sum_{i\in A,j\in B}^{TT\vee TS\vee SS}\delta_\epsilon(r-r_{ij})}\right\rangle_T,$$

where the kernel $\delta_\epsilon(r)$ is a smoothed Dirac delta, $r_{ij}=\|\vec{x}_i(t)-\vec{x}_j(t)\|$, and ϵ is the mean cellular diameter. These correlation functions are shown in Fig. 5 for both the L3.6pl and AsPC1 cases: Panel *A* and panel *C* are made in the presence of the drug, while panel *B* and panel *D* in the absence of the drug. Away from cell-to-cell contact interaction (happening at small *r*, i.e., $\log_2(r)\leq 4.5/4.8$ μm), the relaxation of these correlations is best-fitted with a power-law $C_m(r)\sim A_m r^{\gamma_m}$: The inferred coefficients γ_m^S, γ_m^M, γ_m^T are reported in Tables 1 and 2.

For the L3.6pl case, the main influence of the drug in the metric correlations appears on the mixed ones (tumor–stroma): In this case, the presence of gemcitabine roughly halves the scale factor γ_m^M (i.e., $\gamma_m^M\sim-0.68\rightarrow-0.37$), and this implies a longer correlation length. The whole is in complete agreement with outcomes by maximum entropy analysis (that highlight a raise in the mixed interactions, Fig. 2 panel *H*) and stochastic process theory (that return as the steeper quantifier $D_{S,T}(t)$, Fig. 3 panel *D*). The scale factors γ_m^T, γ_m^S of the other metric correlations (i.e., tumor–tumor and stroma–stroma) change mildly by the presence/absence of the drug (again in agreement with previous outcomes). For the AsPC1 case, the main influence of the drug in the metric correlations gets manifest for the tumor–tumor ones again with a one-half variation of the scale factor γ_m^T (i.e. $\gamma_m^T\sim-0.89\rightarrow-0.48$). Such a slower decay for the correlation function (hence a longer correlation length) is again in agreement with the outcomes of the maximum entropy analysis (Fig. 2*J*) and stochastic process theory (that returns as the steeper quantifier $D_{T,T}(t)$, Fig. 3*F*). The scale factors γ_m^M, γ_m^S of the other correlations (i.e., tumor–stroma and stroma–stroma) change mildly by the presence/absence of the drug (again in agreement with previous outcomes).

Table 1. L3.6pl case

	γ_m (ND | D)		γ_t (ND | D)	
T	-0.84 ± 0.05	-0.80 ± 0.07	-0.39 ± 0.05	-0.44 ± 0.05
M	-0.68 ± 0.05	-0.37 ± 0.07	-0.39 ± 0.02	-0.27 ± 0.02
S	-0.48 ± 0.05	-0.46 ± 0.05	-0.28 ± 0.03	-0.26 ± 0.06

Table 2. AsPC1 case

	γ_m (ND | D)		γ_t (ND | D)	
T	-0.89 ± 0.04	-0.48 ± 0.14	-0.41 ± 0.07	-0.24 ± 0.05
M	-0.85 ± 0.12	-0.96 ± 0.29	-0.42 ± 0.6	-0.48 ± 0.15
S	-0.93 ± 0.12	-0.93 ± 0.21	-0.39 ± 0.10	-0.33 ± 0.15

The topological correlation function measures the reciprocal influence of all cell's couples of types T, M, and S that lie within a neighborhood built by the closer *n* cells and it is defined as

$$C_t^{T\vee M\vee S}(n)=\left\langle \frac{\sum_{i\in A,j\in B}^{TT\vee TS\vee SS}\hat{n}_i(t)\cdot\hat{n}_j(t)\delta_{j,N_n(i)}}{\sum_{i\in A,j\in B}^{TT\vee TS\vee SS}\delta_{j,N_n(i)}}\right\rangle_T,$$

where

$$\delta_{j,N_n(i)}=\begin{cases}1 & \text{if } j \text{ is the } n\text{-neighbor of } i,\\ 0 & \text{otherwise.}\end{cases}$$

These correlation functions are shown in Fig. 5 for both the L3.6pl and AsPC1 cases: Panel *E* and panel *G* are made in the presence of the drug, while panel F and panel H in the absence of the drug. Their behavior is again comparable with a scale-free relaxation, and best-fits have been performed with $C_t(n)=A_t n^{\gamma_t}$: The scale factors γ_t^T, γ_t^M, γ_t^S are reported in the Tables 1 and 2. Considerations similar to those pertaining to the metric case can be drawn.

Finally, as both metric and topological correlation functions can be reasonably fitted by power-laws, but metric's fits are less robust, to confirm their behavior and inspect whether interactions ruling a cell's coordination are dominated by one type or the other (33), we provide a scaling argument. At first, we note that there exists roughly a factor two among the two types of scale factors, i.e., $\gamma_m\sim2\gamma_t$ for all the three cases (S, M, T). If both the correlations (metric and topological) are truly scale-free, it should happen that $C_m(r)/C_t(n)$ does not scale, nor in *r* neither in *n*, i.e., $C_m(r)/C_t(n)\propto(r^{\gamma_m}/n^{\gamma_t})\sim const$. To check this behavior, we must find a relation expressing *r* as a function of *n* or vice versa: This dependence can be experimentally accessed as reported in Fig. 5*I* where we show that it sharply happens that $r(n)\propto\sqrt{n}$ for all the cases (S, M, T), all the experiments (drug/no drug), and both the tumor cell lines (L3.6pl and AsPC1). This implies that $C_m(r)/C_t(n)\sim const$, confirming the long range action of both these types of correlations. While this inspection does not rule out any prevalence in the correlations governing the interactions, it ensures that—on the spatial scale captured by the microscope—homogeneity in cellular densities is enough to justify the mean field nature of the maximum entropy inference. As a last remark, we note that, despite homogeneity, cellular density is not strictly constant; Fig. 5*J*. In particular, this plot

shows peaks at the mean cellular diameter (possibly highlighting the formation of lumps by contact interactions), and the more pronounced case—measured by the steepness of the function in the origin—is the L3.6pl case in the drug setting, while the less pronounced one is the AsPC1 case, still in the drug setting (again in agreement with previous findings): We deepen this point in the last section of *SI Appendix*.

Discussion

We applied an in vitro experimental system, resembling a part of the stromal microenvironment, to study stroma–cancer pancreatic kinetics interactions. By time-lapse confocal imaging, we tracked tumor and stroma cells cocultured in the presence (or in the absence, for comparison) of a chemotherapeutic agent (gemcitabine): The resulting datasets, storing cells' positions and velocities, supplied sufficient information to infer the effect of the drug on stroma–cancer kinetics, as well as their dynamical cross talk, due to a computational algorithm. Focusing on cells' velocities, we analyzed the directions and moduli of these vectors separately: The former were investigated via maximum-entropy inference; the latter were studied via stochastic processes. Further, a third analysis of their correlations ensured global consistency, the whole resulting in a unified synergistic approach for quantifying cells' dynamics and interactions.

By performing the same analysis with and without gemcitabine on two different tumor lines, L3.6pl and AsPC1, we quantified the effect of the drug on their dynamics. We found that, for the L3.6pl cells, gemcitabine highly increased heterotypic interactions (i.e., tumor–stroma), much more than homotypic interactions, that are almost left invariant for the tumor and actually diminished for the stroma. As a result of such enhanced interactions, cells tended to form clusters and, locally, the dynamics of the involved cells turned ballistic, resulting in marked acquired motility. In the AsPC1 cells, instead, the effect of the drug was sensibly milder, nor were mixed interactions raised; neither their dynamics acquired enhanced motility. Correlating these results with counts on dead/live cells, we conclude that in the L3.6pl scenario, the drug killed roughly ∼50% of the cancerous cells without affecting the vitality of the stroma, but the same did not happen in the AsPC1 case.

Focusing on research aspects, these findings contribute to an increase in the number of techniques (integrating those mainly -omics derived) available to quantify drug response to cancer. Focusing on clinical aspects, as stroma can play a very broad critical role—ranging from cancer fighter to cancer facilitator—our method could help (at a very cheap cost) to quickly understand whether the stroma–tumor interaction harms the therapy or not.

Methods

Cell Cultures. PDAC cell lines, i.e., L3.6pl, AsPC1, and pancreatic stellate cells, i.e., PSCs, were grown in DMEM supplemented with 10% fetal bovine serum (FBS) and 1% of penicillin–streptomycin (all from Sigma-Aldrich). Cells were maintained in a humidified environment with 5% CO_2 at 37 °C and were passaged at ∼80% confluency.

Wound-Healing Assay. Six-well plates were incubated with 0.01 mg/ml of fibronectin (Sigma-Aldrich) for 30 min at 37 °C before rinsing with phosphate-buffered saline (PBS, Invitrogen). Each well was seeded with $5 \cdot 10^5$ PSCs and maintained at 37 °C and 5% CO_2 for 24 h to allow cell adhesion and the formation of a confluent monolayer. These confluent PSC monolayers were scratched with 10-μL pipette tips to create a wound, and then, the medium was removed and replaced with a fresh low-serum-supplemented culture medium (1% FBS, control) or with a conditioned medium (conditioned for 48 h) which had been generated from AsPC1 or L3.6pl. All scratch assays were performed in quadruplicate. Quantification of the wound area was performed with the wound-healing size tool, an ImageJ plugin (34).

Tumor–Stroma Staining and Coculture. To distinguish the two cell populations and to identify the precise position of cells in order to track them, the CellMask^{TM} Deep Red Plasma Membrane Stain (Invitrogen^{TM}) was used to mark tumor cell cytoskeleton (false-colored in red in Fig. 1 *A* and *B*), while nuclei of both cell lines were marked with Hoechst 33342 (Sigma-Aldrich) (false-colored in green in Fig. 1 *A* and *B*). In detail, CellMask^{TM} Deep Red was diluted in order to reach a concentration of 5 μg/mL and was added to cell media for 15 min before washing; Hoechst 33342 was diluted at 200 μg/ml and incubated with cells for 30 min before washing. Once stained, the living cells were mixed according to the ratio found in physiological tumors, i.e., 25% of tumor cells versus 75% of stroma cells. In detail, 15.000 cancerous cells (L3.6pl or AsPC1) and 45.000 PSCs were cocultured within a well of a 8-well chamber slide (IBIDI). When moved to the confocal microscope, cells were incubated with L15 medium (Life Technologies), that is properly designed for supporting cell growth in environments without CO_2 equilibration. Of note, we used a phenol red-free media, to reduce background fluorescence.

Drug Treatment. To analyze the effects of anticancer drugs on tumor–stroma cross talk, we performed the same experiments by treating the cells with gemcitabine. To this aim, gemcitabine HCl (supplied by Selleckchem) was diluted in DMEM (or in L15 medium just before confocal laser scanning microscopy) at 5 μM final concentration.

Time-Lapse Confocal Laser Scanning Microscopy. Confocal laser scanning microscopy (CLSM) was performed with a Leica TCS SP8 (Leica Microsystems GmbH, Wetzlar, Germany) microscope (objective HC PL APO CS2 40x/1.30 OIL). Time-lapse CLSM was carried out after 48 h of coculture for 10 consecutive hours. To this aim, 10 h of acquisitions were collected, each one composed of 60 time frames (one acquisition every 10 min); each acquisition was constituted by 16 neighboring regions (4 × 4 matrix) and a 25-μm-thick Z-stack with a z-step value of 1 μm.

Cell Counting. For these experiments, long-term staining was carried out by transfections with Lipofectamine 2000 (Invitrogen^{TM}). L3.6pl, AsPC1 cells, and PSCs were transfected with 100 ng of mCherry–zeocin or GFP–puromycin vectors and selected with zeocin and puromycin, respectively, for all the culturing time, in order to generate red L3.6pl or AsPC1 (mCherry) and green PSCs (GFP) cells. The transfection was performed following the manufacturer's instructions. All the experiments were conducted by coculturing 30.000 L3.6pl cells with 90.000 PSCs in a 24-well plate for 0, 48, and 58 h, in the presence or absence of 5 μM gemcitabine. Then, bright-field and fluorescence microscope acquisitions were performed to visualize the cell morphology. Images were acquired at room temperature using a LEICA DM6000 inverted microscope (Leica) on a DC 350 FX camera (Leica).

FACS analyses at the indicated time points were performed. The nuclei of all cell lines were marked with Hoechst 33342 (Sigma-Aldrich). After sorting, the red (L3.6pl and AsPC1) and green (PSCs) cells were manually (hemocytometer) or automatically (FACS) counted.

Samples ($n > 6$) were run on the FACS Canto II (BD). Results for continuous variables are presented as means ± standard deviation (SD) of at least three independent experiments. Treatment groups were compared with the independent samples t test. $P < 0.05$ was considered statistically significant. All analyses were performed using GraphPad Prism7.

We refer to *SI Appendix* to deepen the theoretical and computational aspects of the research as well as all the statistical details.

Data, Materials, and Software Availability. Code and data-sets are available as *SI Appendix*.

ACKNOWLEDGMENTS. The authors gratefully acknowledge the ERC Starting Grant INTERCELLMED (project number 759959), the My First AIRC Grants (MFAG-2019, project number 22902; MFAG-2017, project number 20206), Ministero degli Affari Esteri e della Cooperazione Internazionale (BulBul grant Italy–Israel, CUP: F85F21006230001), "Tecnopolo per la medicina di precisione" (TecnoMed Puglia)–Regione Puglia: DGR n.2117 del 21/11/2018, CUP: B84I18000540002, "Tecnopolo di Nanotecnologia e Fotonica per la medicina di precision" (TECNOMED)–FISR/MIUR-CNR: delibera CIPE n.3449 del 7-08-2017, CUP: B83B17000010001. F.A. and A.F. acknowledge also PON *R&I* ARS01-00876 "BIO-D-Sviluppo di Biomarcatori Diagnostici per la medicina di precisione e la terapia personalizzata" and Sapienza University of Rome (CUP: RM120172B8066CB0).

Author affiliations: [a]Institute of Nanotechnology, National Research Council, Lecce 73100, Italy; [b]Dipartimento di Matematica e Fisica Ennio De Giorgi, Università del Salento, Lecce 73100, Italy; [c]Institute of Genetics and Biophysics Adriano Buzzati-Traverso, CNR, Naples 80131, Italy; [d]Dipartimento di Matematica Guido Castelnuovo, Sapienza Università di Roma, Rome 00185, Italy; and [e]Istituto Nazionale di Fisica Nucleare, Sezione di Lecce, Lecce 73100, Italy

Author contributions: E.L., A.B., and L.L.d.M. designed research; F.A., M.C., D.D.C., A.F., R.R., E.D., and G.G. performed research; F.A., A.F., R.R., E.D., E.L., A.B., and L.L.d.M. analyzed data; and E.L., A.B., and L.L.d.M. wrote the paper.

1. S. Vedel *et al*., Migration of cells in a social context. *Proc. Natl. Acad. Sci. USA* **110**, 129–134 (2013).
2. R. Axelrod, K. J. Pienta, Cancer as a social dysfunction: Why cancer research needs new thinking. *Mol. Can. Res.* **16**, 1346–1347 (2018).
3. J. H. Lee *et al*., Microfluidic co-culture of pancreatic tumor spheroids with stellate cells as a novel 3D model for investigation of stroma-mediated cell motility and drug resistance. *J. Exp. Clin. Can. Res.* **37**, 1–12 (2018).
4. S. Sebens, H. Schafer, The tumor stroma as mediator of drug resistance-a potential target to improve cancer therapy? *Curr. Pharm. Biotech.* **13**, 2259–2272 (2012).
5. E. S. Nakasone *et al*., Imaging tumor-stroma interactions during chemotherapy reveals contributions of the microenvironment to resistance. *Cancer Cell* **21**, 488–503 (2012).
6. A. Neesse *et al*., Stromal biology and therapy in pancreatic cancer. *Gut* **60**, 861–868 (2011).
7. D. Thomas, P. Radhakrishnan, Tumor-stromal crosstalk in pancreatic cancer and tissue fibrosis. *Mol. Cancer* **18**, 1–15 (2019).
8. E. Lonardo *et al*., Pancreatic stellate cells form a niche for cancer stem cells and promote their self-renewal and invasiveness. *Cell Cycle* **11**, 1282–1290 (2012).
9. R. F. Hwang *et al*., Cancer-associated stromal fibroblasts promote pancreatic tumour progression. *Cancer Res.* **68**, 918–926 (2008).
10. M. Amrutkar *et al*., Secretion of fibronectin by human pancreatic stellate cells promotes chemoresistance to gemcitabine in pancreatic cancer cells. *BMC Cancer* **19**, 1–16 (2019).
11. P. P. Provenzano *et al*., Enzymatic targeting of the stroma ablates physical barriers to treatment of pancreatic ductal adenocarcinoma. *Cancer Cell* **21**, 418–429 (2012).
12. J. Gore, M. Korc, Pancreatic cancer stroma: Friend or foe? *Cancer Cell* **25**, 711–712 (2014).
13. B. C. Ozdemir *et al*., Depletion of carcinoma-associated fibroblasts and fibrosis induces immunosuppression and accelerates pancreas cancer with reduced survival. *Cancer Cell* **25**, 719–734 (2014).
14. A. D. Rhim *et al*., Stromal elements act to restrain, rather than support, pancreatic ductal adenocarcinoma. *Cancer Cell* **25**, 735–747 (2014).
15. M. Apte *et al*., A starring role for stellate cells in the pancreatic cancer microenvironment. *Gastroenterology* **144**, 1210–1219 (2013).
16. M. J. Ware *et al*., Generation of an in vitro 3D PDAC stroma rich spheroid model. *Biomaterials* **108**, 129–142 (2016).
17. E. Tomas-Bort *et al*., 3D approaches to model the tumour microenvironment of pancreatic cancer. *Theranostics* **10**, 5074 (2020).
18. E. Armingol *et al*., Deciphering cell-cell interactions and communication from gene expression. *Nat. Rev. Gen.* **22**, 71–88 (2021).
19. L. De Monte *et al*., Intratumor T helper type 2 cell infiltrate correlates with cancer-associated fibroblast thymic stromal lymphopoietin production and reduced survival in pancreatic cancer. *J. Exp. Med.* **208**, 469–478 (2011).
20. E. Schneidman *et al*., Weak pairwise correlations imply strongly correlated network states in a neural population. *Nature* **440**, 1007–1012 (2006).
21. W. Bialek *et al*., Statistical mechanics for natural flocks of birds. *Proc. Natl. Acad. Sci. U.S.A.* **109**, 4786–4791 (2012).
22. E. Agliari *et al*., A statitical-inference approach to reconstruct intercellular interactions in cell migration experiments. *Sci. Adv.* **6**, 11 (2020).
23. S. Cocco *et al*., Inverse statistical physics of protein sequences: A key issues review. *Rep. Prog. Phys.* **81** (2018).
24. J. A. Acebron *et al*., The Kuramoto model: A simple paradigm for synchronization phenomena. *Rev. Mod. Phys.* **77**, 137 (2005).
25. J. Skilling, *Maximum Entropy and Bayesian Methods* (Springer Science, Cambridge, 2013).
26. U. Tavoni *et al*., Functional coupling networks inferred from prefrontal cortex activity show experience-related effective plasticity. *Netw. Neurosci.* **1**, 275–301 (2017).
27. H. C. Nguyen, R. Zecchina, J. Berg, Inverse statistical problems: From the inverse Ising problem to data science. *Adv. Phys.* **66**, 197–261 (2017).
28. M. J. Wainwright, M. I. Jordan, Graphical models, exponential families, and variational inference. *Found. Trends Mach. Learn.* **1**, 1–305 (2008).
29. G. Auletta, F. Rondoni, A. Vulpiani, The relevance of the maximum entropy principle in non-equilibrium statistical mechanics. *Europ. Phys. J. Spec. Top.* **226**, 2327–2343 (2017).
30. E. Agliari *et al*., Cancer driven dynamics of immune cells in a microfluidic environment. *Sci. Rep.* **4**, 6639 (2014).
31. A. Cavagna *et al*., Scale-free correlations in starling flocks. *Proc. Natl. Acad. Sci. U.S.A.* **107**, 11865–11870 (2010).
32. M. Ballerini *et al*., Interaction ruling animal collective behavior depends on topological rather than metric distance: Evidence from a field study. *Proc. Natl. Acad. Sci. U.S.A.* **105**, 1232–1237 (2008).
33. H. Failmezger *et al*., Topological Tumor Graphs: A graph-based spatial model to infer stromal recruitment. *Cancer Res.* **80**, 1199–1209 (2020).
34. A. Suarez-Arnedo *et al*., An image J plugin for the high throughput image analysis of in vitro scratch wound healing assays. *PLoS One* **15**, e0232565 (2020).